APPLIED SCIENCES AND ENGINEERING

Albumin-chaperoned cyanine dye yields superbright NIR-II fluorophore with enhanced pharmacokinetics

Rui Tian[1]*, Qiao Zeng[2]*, Shoujun Zhu[1†‡], Joseph Lau[1], Swati Chandra[1], Robert Ertsey[3], Kenneth S. Hettie[3§], Tarn Teraphongphom[3], Zhubin Hu[4], Gang Niu[1], Dale O. Kiesewetter[1], Haitao Sun[4†], Xiaodong Zhang[5], Alexander L. Antaris[6], Bernard R. Brooks[2], Xiaoyuan Chen[1†]

NIR-II fluorescence imaging greatly reduces scattering coefficients for nearly all tissue types at long wavelengths, benefiting deep tissue imaging. However, most of the NIR-II fluorophores suffer from low quantum yields and/or short circulation time that limit the quality of NIR-II imaging. Here, we engineered a supramolecular assembly of protein complex with lodged cyanine dyes to produce a brilliant NIR-II fluorophore, providing a NIR-II quantum yield of 21.2% with prolonged circulation time. Computational modeling revealed the mechanism for fluorescence enhancement and identified key parameters governing albumin complex for NIR-II fluorophores. Our complex afforded high-resolution microvessel imaging, with a 3-hour imaging window compared to 2 min for free dye alone. Furthermore, the complexation strategy was applied to an antibody-derived assembly, offering high-contrast tumor imaging without affecting the targeting ability of the antibody. This study provides a facile strategy for producing high-performance NIR-II fluorophores by chaperoning cyanine dyes with functional proteins.

INTRODUCTION

Near-infrared (NIR) fluorescence imaging has gained popularity in the medical community because of its applicability for intraoperative imaging. This noninvasive imaging modality, also termed NIR-I imaging because of its range of 700 to 1000 nm, has high sensitivity, as fluorophores can be repeatedly excited by tissue-penetrating NIR light (*1*). It compares favorably with techniques such as nuclear imaging with radionuclides, which is the current clinical standard for molecular imaging (*1*). In addition, low toxicity imaging probes allow for prolonged imaging and/or repeated scanning over time. Moreover, the contrast from fluorescence emission enables clear visualization of target tissue from surrounding tissues. Last, this technique has the potential to be integrated with other imaging modalities—such as photoacoustic imaging, ultrasound imaging, magnetic resonance imaging, and positron emission tomography imaging—to achieve multimodal imaging platforms (*2*). Proposed applications of NIR imaging include angiography, delineation of tumors and metastases, and imaging of lymphatic vessels. Thus far, few NIR dyes, such as indocyanine green (ICG) and methylene blue, are approved by the U.S. Food and Drug Administration for investigational human studies (*3*). ICG has been used clinically for cardiovascular function test and retinal angiography. While promising, NIR imaging is still encumbered by drawbacks such as high photon attenuation, tissue autofluorescence, and light scattering.

NIR-II imaging, which ranges from 1000 to 1700 nm, offers a promising solution to these limitations (*4*–*7*). This imaging modality provides greater penetration and contrast compared to its NIR-I counterpart; however, present fluorophores have limited translational potential (*8*, *9*). For example, NIR-II fluorophores derived from inorganic nanoparticles and carbon nanotubes demonstrate biocompatibility and safety concerns. In addition, other typical NIR-II fluorophores such as donor-acceptor-donor (D-A-D) dyes have low quantum yields (QYs) (*10*). Although prolonging the conjugated structure of polymethine structures produced efficient NIR-II fluorophores, few of them are water soluble or biocompatible (*11*). Thus, the primary barrier to clinical translation for NIR-II imaging is the limited number of fluorophores that satisfy brightness and biocompatibility requirements (*12*).

For this reason, the use of off-peak cyanine dyes has been suggested for NIR-II imaging (*13*–*16*). These dyes have an emission spectrum that spans the entire NIR-I region, with an emission tail that extends into the NIR-II window. Because of this property, selected NIR-I probes can be repurposed for NIR-II bioimaging, thus accelerating the pathway to clinical translation of this imaging modality (*17*). In addition to offering high-contrast tumor and vessel imaging, these dyes also show rapid hepatobiliary clearance, thus reducing issues related to biocompatibility and safety compared with inorganic probes. However, these dyes afford an imaging window of less than 2 min for vessel imaging because of the short circulation time (*15*, *16*, *18*, *19*). The bioconjugation of these dyes with proteins could provide enhanced circulation time, although this may come at the expense of brightness due to a quenching effect. We recently reported the conjugation of a NIR-II fluorophore with Erbitux, a ligand for the epidermal growth factor receptor (EGFR) to image the high EGFR expression tumor (*15*). However, it is still a challenge to develop a bright NIR-II fluorophore with high QY and improved pharmacokinetic profile. We hypothesize that tailoring the supramolecular assemblies of protein complexes with a lodged NIR-II dye will achieve high-quality NIR-II imaging (*13*, *20*).

[1]Laboratory of Molecular Imaging and Nanomedicine, National Institute of Biomedical Imaging and Bioengineering (NIBIB), National Institutes of Health, Bethesda, MD 20892, USA. [2]Laboratory of Computational Biology, National Heart, Lung and Blood Institute, National Institutes of Health, Bethesda, MD 20892, USA. [3]Department of Otolaryngology, Stanford University, Stanford, CA 94305, USA. [4]State Key Laboratory of Precision Spectroscopy, School of Physics and Materials Science, East China Normal University, Shanghai 200062, P. R. China. [5]Department of Physics, School of Science, Tianjin University, Tianjin 300354, P. R. China. [6]Intuitive Surgical, Kifer Rd., Sunnyvale, CA 94086, USA.
*These authors contributed equally to this work.
†Corresponding author. Email: sjzhu@jlu.edu.cn (S.Z.); shawn.chen@nih.gov (X.C.); htsun@phy.ecnu.edu.cn (H.S.)
‡Present address: Institute of Translational Medicine, The First Hospital; State Key Laboratory of Supramolecular Structure and Materials College of Chemistry, Jilin University, Changchun 130021, China.
§Present address: Department of Radiology, Stanford University, Stanford, CA 94305, USA.

The present study investigates whether the assembly of off-peak cyanine dyes with bovine serum albumin (BSA) will allow for increased circulation time, QY, stability, and imaging contrast. Through experimentations and computational modeling, we identified a self-assembling IR-783@BSA ~50 nm in size that showed high stability and fluorescence intensity suitable for high-contrast imaging. The enhanced circulation time of IR-783@BSA enabled the visualization of sub–3-μm-wide blood vessels up to 3 hours post-injection (p.i.), with a super high contrast. The nanomolar binding affinity interaction between IR-783 and albumin enhanced the twisted intramolecular charge transfer (TICT) process and NIR-II QY production. By engineering the supramolecular assemblies between albumin and the cyanine dye, the complex can hold the twisted conformation and enable the enhancement of the TICT process and circulation time. We further demonstrated that this approach can be extended to a monoclonal antibody (Erbitux) to confer molecular targeting properties. This study provides a facile strategy for producing high-performance NIR-II fluorophores by chaperoning cyanine dyes with functional proteins, which shows high potential in clinical settings.

RESULTS

Cyanine dyes exhibit improved fluorescence in the presence of albumin

As shown in Fig. 1A, our design involves the assembly of cyanine dyes with BSA via supramolecular interactions to create a stable fluorophore@BSA complex. Hence, we first evaluated three candidates, IR-783, IR-12N3, and ICG, since they were previously determined to have higher NIR-II QY compared with other cyanine dyes (the relative QY of IR-12N3 is 2.8-fold higher than that of ICG in BSA buffer) (*15*). For the protein component, we choose albumin since it is an endogenous protein with a long biological half-life (19 days) and it has been used clinically as a drug carrier (e.g., Abraxane) (*21*, *22*). Then, we investigated the interaction between cyanine dyes with BSA and determined the very strong binding affinity with the K_d (dissociation constant) value of 1 nM (Fig. 1B) (*23*). The relative NIR-I QY of IR-783 was nearly comparable with IR-12N3 (fig. S1) (*15*). Next, temperature dependence of the fluorophores was tested by heating each dye to temperatures ranging from room temperature to 90°C in the presence of BSA. Fluorescence intensity increased approximately sixfold at temperatures near 60°C (Fig. 1C and fig. S1D). The linear relationship between the concentration of dyes and fluorescence intensity was found to be less than 4 μM (fig. S1E). Further testing the fluorescence enhancement in fetal bovine serum (FBS) (undiluted FBS with a concentration of ~0.75 mM), we confirmed that the fluorescence of free dye is very sensitive in FBS at low concentration (e.g., 0.4 μM; fig. S1, F and G). Because of the TICT of cyanine dyes (*15*, *17*), IR-783 also exhibited bright NIR-II tail emission, encouraging us to optimize the NIR-II emission of the as-prepared complex for deep tissue imaging (Fig. 1D).

Fluorescence intensity of the IR-783@BSA complex is dependent on molar ratio, incubation time, and temperature

We manufactured the complexes using four well-designed synthetic strategies (conditions 1 to 4 in fig. S2A). The first condition (C1) involved freely mixing the dye with BSA and applying heat for 10 min to form the complex. The second (C2) included glutathione (GSH) in addition to 10-min heating, with GSH facilitating the reversible breakage of disulfide bonds to entrap the fluorophores. The third (C3) involved the addition of GSH and glutaraldehyde (GTD), a cross-linking agent for primary amines, as well as 10-min heating. Last, the fourth (C4) refers to the combination of GTD and 10-min heat. Before we further optimized the formation conditions for the fluorophore@BSA complex, we developed a ratio using the FBS/PBS (phosphate-buffered saline) buffer method to test the stability of the complex by monitoring the fluorescence intensity. Specifically, the fluorescence intensity of all the tested fluorophores is higher in FBS than in BSA; as a result, the fluorescence ratio of a fluorophore in FBS/PBS closest to 1 indicates the highest stability with the BSA cage, while the fact that it deviates from 1 indicates that free dye has escaped from the BSA cage. We next measured the fluorescence intensity, size, and stability of the three fluorophore@BSA complexes obtained from the above four methods (C1 to C4). The IR-783@BSA complex was more stable compared with the IR-12N3@BSA and ICG@BSA complexes (Fig. 1E and fig. S2, B to D). In addition, the IR-783@BSA complex also showed the highest QY and greatly higher fluorescence enhancement after heating at 60°C compared to the other two fluorophore@BSA complexes. Thus, we chose the IR-783@BSA for further optimization.

As shown in fig. S2E, the optimization procedures involved optimizing the ratio and concentration of dye and albumin, preincubation time after mixing them, and temperatures for 10-min heat (from room temperature to 70°C) after the incubation, as well as optimizing the stability and size for a good performance in both fluorescence intensity and in vivo pharmacokinetics. We first optimized the concentration dependence of IR-783 for both freely mixed (C1) and GSH conditions (C2), substantiating the ratio up to 1:1 for BSA:IR-783 with optimized properties, such as size, fluorescence intensity, and complex stability (fig. S3, A to F). The concentration of the reaction system was controlled at less than 20 mg/ml to avoid aggregation and over–cross-linking. The preincubation time was optimized to 24 hours by measuring both the stability and the size of the complex at different incubational time points (fig. S3, G to H). Three different ratios of BSA:IR-783 were tested at each of the four methods to further optimize stability and emission brightness. We observed that the complexes were most stable at ratios of BSA:dye of 1:0.5 and 1:1, with the complex becoming less stable at a ratio of 1:2 (fig. S4, A to F).

On average, the size of the complex was ~60 nm for the GSH (C2) and GSH + GTD (C3) conditions, while it was less than 20 nm for the freely mixed (C1) and GTD (C4) conditions, indicating that the GSH method led to intermolecular cross-linking (fig. S4, G to L). Transmission electron microscopy, atomic force microscopy, and electrophoresis analysis also indicated that C2 and C3 yielded larger-size complexes as compared with C1 and C4 (Fig. 1F and fig. S4, M to P). From the electrophoresis analysis, we observed monomer, dimer, trimer, and other multimers of the nanocomplex. Thus, density gradient centrifugation (DGU) purification was needed to separate the complex from the smaller species to obtain uniform-size complexes. In addition, the temperature of 10-min heat is also important to form the stable complex, demonstrating that 60° and 70°C met the need for tailoring the large complex, and the higher temperature can produce a larger population of a large nanocomplex (Fig. 1G).

Complexation between cyanine dye and albumin enhances TICT

Understanding the mechanism of interaction between IR-783 and albumin is critical to guide efficient nanocomplex synthesis and

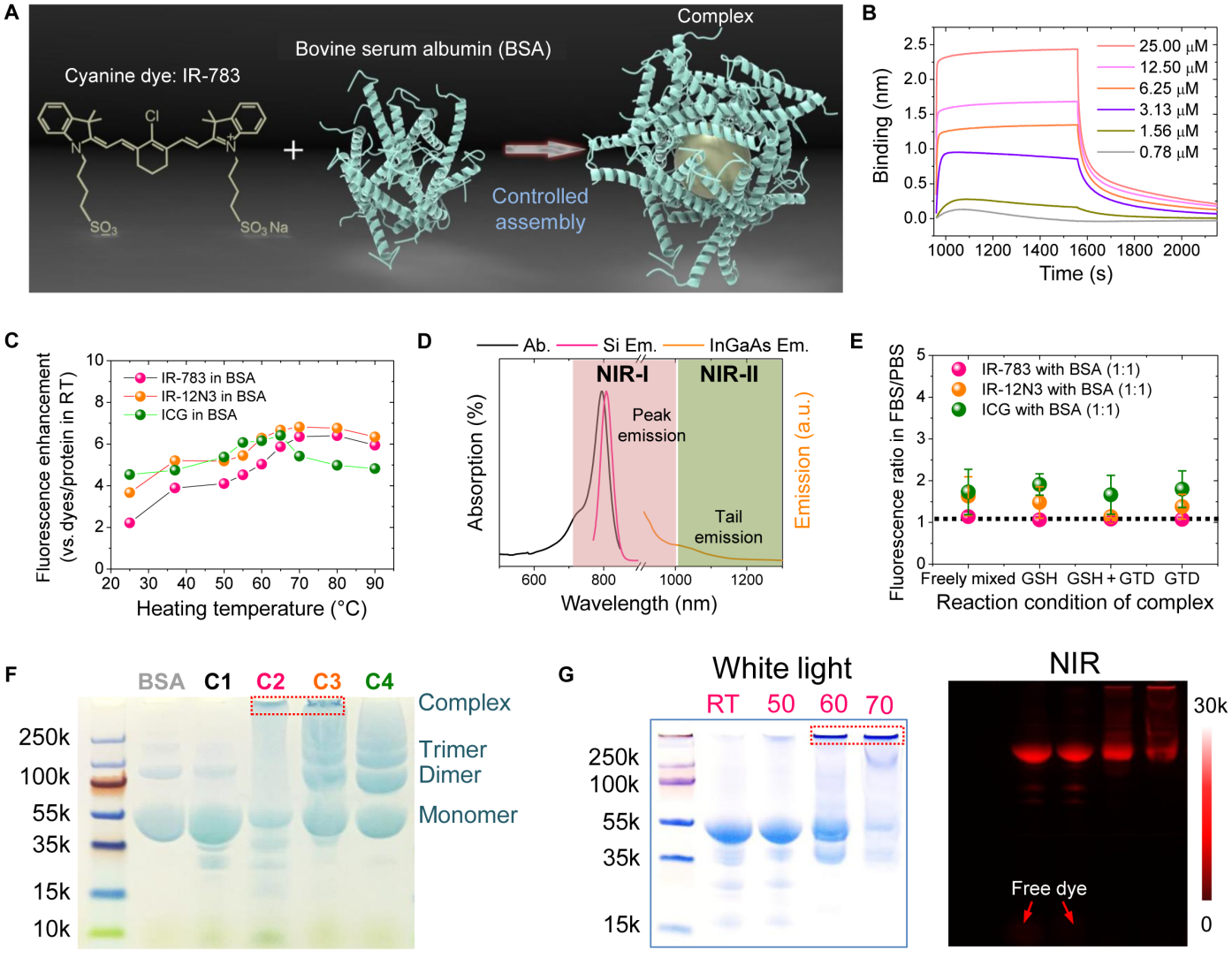

Fig. 1. Optimization of the assembly between cyanine dyes and albumin produced an efficient NIR-II complex. (**A**) Simplified design for the formation of the fluorophore@BSA complex. (**B**) Kinetic binding assay of IR-783 to albumin was measured by biolayer interferometry with K_d value ~1 nM. (**C**) Brightness enhancement after heating for 10 min of dyes premixed with BSA (100 μM). (**D**) Absorption and NIR-I and NIR-II emission of IR-783 in 100 μM BSA solution. Ab., absorption spectra; Si Em., emission spectra recorded on silicon camera; InGaAs Em., emission spectra recorded on InGaAs camera. (**E**) Fluorescence enhancement of the fluorophore (IR-783, IR-12N3, and ICG) @BSA complex (1:1 ratio) at 60°C. The IR-783:BSA complex is the most stable, with a fluorescence ratio closest to 1. GTD, glutaraldehyde. (**F**) Electrophoresis analysis of IR-783@BSA complexes (C1 to C4 were synthesized with 10-min posttreatment at 60°C). C2 and C3 have a large population close to the top compared with C1 and C4. (**G**) Electrophoresis gel analysis of IR-783@BSA complexes [prepared from C2: glutathione (GSH) and heat] with 10 min posttreatment at different temperatures [room temperature (RT), 50°, 60°, and 70°C]. At higher temperatures, a higher–molecular weight complex was observed.

fluorescence enhancement. We performed docking modeling to investigate the poses and interaction between IR-783 and albumin (Fig. 2, A and B) (*22*). The binding site of IR-783 was identified as the cleft of albumin (Fig. 2A). Although both IR-783 and ICG were assigned to the similar binding sites of albumin, ICG exhibited a higher tendency for self-assembly (Fig. 2, C and D, and fig. S5, A to E). The deviation of self-assembly behavior suggests the different tendencies between two competing reactions, which are the dye molecule self-assembly and the dye-albumin binding interaction. Next, we removed the disulfide bonds to simulate the partially denatured albumin after GSH treatment. The optimal conformation was acquired from the equilibrium modeling for further docking with IR-783 (*24*, *25*). The generated binding poses exhibited very strong π-π stacking between IR-783 [shown in purple (Fig. 2E)] and the Trp^{214} of albumin [shown in green (Fig. 2E)], especially for the most energetically favorable binding pose (the highest binding affinity was estimated as −9.2 kcal/mol) (fig. S5F). Tryptophan (Trp) has the largest conjugate system among all the amino acid residues in albumin. The highest occupied molecular orbital–lowest unoccupied molecular orbital (HOMO-LUMO) gap is usually smaller when the conjugate system is larger, especially when the molecule has a π-π interaction with a nearby molecule (Fig. 2E). The distance between their facing aromatic rings was predicted to be 3.761 Å, indicating a very short distance for a strong electronic coupling. The strong interaction between IR-783 and the Trp^{214} held the twisted conformation of the IR-783, enabling the enhancement of the TICT process and NIR-II QY (*26*, *27*). The enhanced

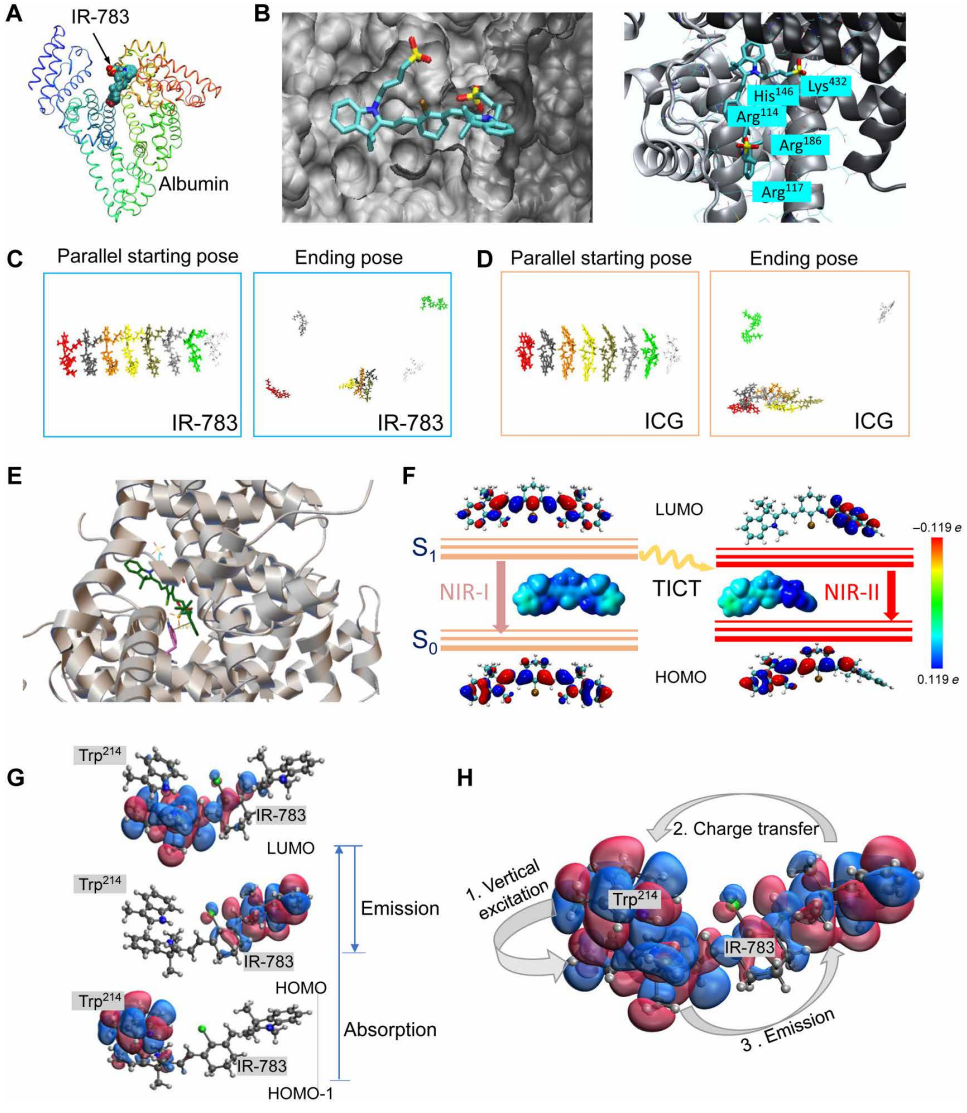

Fig. 2. The possible interaction mechanism between IR-783 and albumin is critical to guide efficient nanocomplex synthesis and fluorescence enhancement. (**A**) Docking modeling for the IR-783@albumin complex. (**B**) Details of binding residues and active pocket between IR-783 and albumin. (**C** and **D**) The intermolecular stacking of IR-783 and ICG. ICG showed relatively higher tendency to be self-assembling compared with IR-783. (**E**) Docking modeling for IR-783 and albumin with partial disulfide bond cleavage, affording strong interaction between IR-783 and the Trp residue of albumin. (**F**) Schematic illustration of the transformation of TICT induced NIR-I and NIR-II states of IR-783, including the HOMOs and LUMOs and the ESP maps that are plotted using the color range from red [−0.119 electron (*e*), negative] to blue (0.119 electron, positive). S_0, ground state; S_1, excited state. (**G**) The LUMO (top), HOMO (middle), and HOMO-1 (bottom) are the three major molecular orbitals involved in the absorption (HOMO-1 → LUMO) and emission (LUMO→HOMO) processes. HOMO-1 lies on the indole ring of Trp^{214}, while LUMO and HOMO are lying on the closer and further side of IR-783 with respect to Trp^{214}. (**H**) The absorption and emission form a cycle with three steps: (1) vertical excitation (HOMO-1 → LUMO), (2) charge transfer from IR-783 to Trp^{214} (HOMO → HOMO-1), and (3) emission (LUMO → HOMO).

TICT process was further supported by time-dependent density functional theory (TDDFT) calculations at the tuned LC-BLYP*/6-31G(d) level (see the Supplementary Materials for computational details) (*15*, *28*). The corresponding HOMOs, LUMOs, and maps of electrostatic potential (ESP) surfaces are plotted in Fig. 2F and fig. S5 (G and H). For the NIR-I emission process, the calculated fluorescence wavelength was 775 nm, which was in agreement with the experimentally measured value of 800 nm (fig. S5I). Both the HOMOs and LUMOs distributed along the whole molecular backbone, which suggested a strong π-to-π* local excitation emission. According to the docking modeling with the best-established binding pose between IR-783 and albumin, the rotation of the indoline moiety (with a dihedral angle of 90°) created an asymmetric π-conjugated backbone that resulted in charge redistribution and further induced the TICT (Fig. 2F). The calculated fluorescence wavelength increased to ~1433 nm, which corresponded to the NIR-II emission observed in our study (from 1000 to 1500 nm).

Furthermore, because of the short distance (<4 Å) between IR-783 and Trp^{214}, we extended the system to a cluster consisting of IR-783 and Trp^{214} of albumin using the same method for computing excitation energy to understand the high QY in the case of IR-783@BSA. The computational result showed that the vertical excitation involved the transition from HOMO-1 to LUMO, where HOMO-1 almost lies

on the indole ring of Trp^{214} and LUMO lies on the closer half side of IR-783 with respect to Trp^{214} (Fig. 2G). The emission corresponds to the transition from LUMO to HOMO, where the HOMO lies on the farther side of IR-783 with respect to Trp^{214}. An electronic transition from HOMO (IR-783) to HOMO-1 (Trp^{214}) will happen before final emission. The distance between the centers of HOMO and HOMO-1 is about 12 Å. As the QY is proportional to the lifetime and to the inverse of the transition rate, the long distance between the HOMO and HOMO-1 explains the high QY of IR-783@BSA in the experiment (Fig. 2H and table S1).

The IR-783@BSA complex achieved prolonged circulation due to the albumin motif

After optimizing both brightness and stability properties, we turned to NIR in vivo investigation for further screening. The free cyanine dyes cleared rapidly, limiting the imaging window up to 2 min for vessel imaging (fig. S6, A and B). The IR-783@BSA complex from C2 generated higher contrast for vessel imaging compared to the IR-12N3@BSA and ICG@BSA complexes (fig. S6C). In vivo NIR-I and NIR-II imaging demonstrated a longer imaging time window, up to 1 hour, and higher contrast for the optimized IR-783@BSA complex. This differs sharply from the freely mixed complex which proved unstable, as shown by the high skin uptake of the dye. The free dye showed less contrast and had an imaging time window of only a few minutes with very poor fluorescence intensity (fig. S7A). The IR-783@BSA (C1) and IR-783@BSA-GSH (C2) complexes showed prolonged circulation time and increased contrast, while the C1 complex showed relatively higher skin uptake and lower fluorescence intensity (fig. S7, B to E). In addition, we evaluated the performance of IR-783@BSA complexes treated with GSH, GSH/GTD, and GTD (C2 to C4),

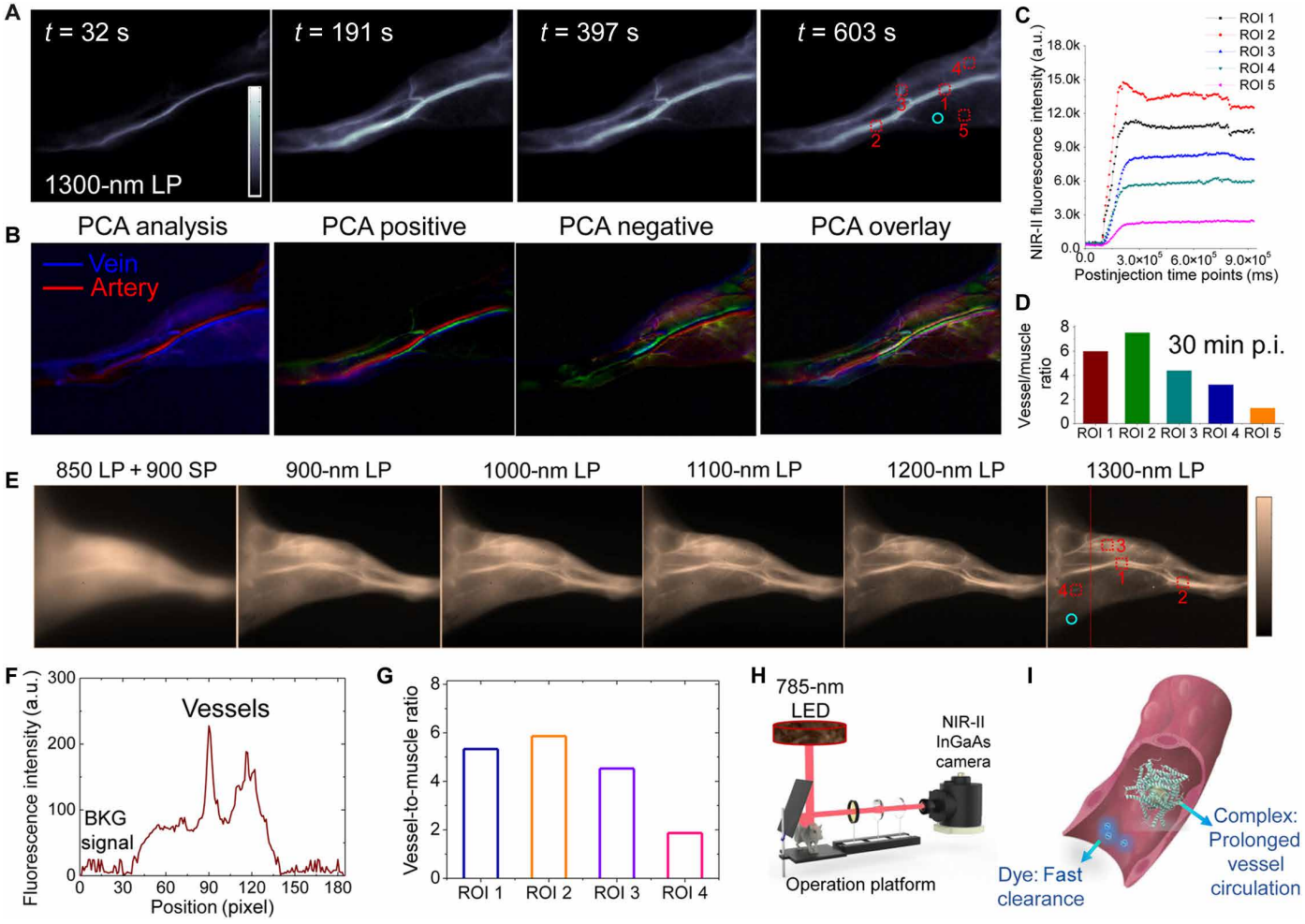

Fig. 3. The IR-783@BSA complex enables high-contrast, real-time NIR-II vessel imaging. (**A**) The recorded NIR-II video of hindlimb vessels in mouse at several time points p.i. of the IR-783@BSA complex at 1300-nm long-pass (LP) filters. (**B**) PCA analysis from the real-time video imaging distinguished both vein and artery vessels, as well as small vessels and background. (**C**) The monitor of fluorescence intensity profile of five selected vessels in NIR-II video imaging of (A). High contrast between the vessel and background is maintained for up to ~30 min in the NIR-II imaging window. The red dotted square is the ROI of vessel, and the cyan circle is the ROI of muscle. a.u., arbitrary units. (**D**) Vessel-to-muscle signal ratio at 30 min p.i. showed high-contrast value up to 6. (**E**) The high brightness of the IR-783@BSA complex affords low-power LED-excited hindlimb imaging at wide NIR-II subwindows. The low-power LED light (10 to 50 mW/cm^2) is more suitable for potential clinical use. The dotted line shows a representative cross-sectional profile of hindlimb. SP, short-pass. (**F**) The cross-sectional intensity profile of hindlimb in (E) (the dotted line). BKG, background. (**G**) LED-excited imaging shows equal vessel-to-muscle signal ratio [ROI 1 to 4 in (E)] with 785-nm laser excited imaging. (**H**) Scheme of LED-excited NIR-II imaging system. (**I**) Scheme of prolonged vessel circulation of the IR-783@BSA complex compared with free IR-783.

respectively, and found that the IR-783@BSA-GSH/GTD complex prolonged the vessel imaging window up to 3 hours compared with the other complexes. The IR-783@BSA-GSH/GTD complex also had faster excretion and lower skin uptake than the other two complexes (fig. S8). Compared with previous syntheses for albumin-derived complexes, the present method affords systematic tuning of circulation time and brightness of applied fluorophores (*29*–*33*).

We then probed the NIR-II QY of the IR-783@BSA complex using IR-E1050 (a typical D-A-D NIR-II fluorophore) and Hipco carbon nanotubes (CNT) as reference compounds (*34*). The QY of IR-783@BSA was ninefold higher than that of IR-E1050 and 53-fold higher than that of Hipco CNT (fig. S9, A and B). NIR-II imaging over NIR-II subwindows (e.g., 1200 and 1300 nm) demonstrated much-improved signal-to-background ratio (SBR) than NIR-I imaging (*35*), indicating that the improved imaging really benefits from both contrast and circulation time of the developed imaging agents (fig. S9, C to F).

The IR-783@BSA complex enabled high-resolution and high-contrast blood vessel imaging

We subsequently performed high-contrast, real-time NIR-II vessel imaging using the optimized IR-783@BSA complex. The recorded NIR-II video of hindlimb vessels in mouse produced supercontrast vessel imaging over the 1300-nm sub–NIR-II window (Fig. 3A). Principal components analysis (PCA) was applied to the real-time video imaging to differentiate venous and arterial vessels, benefiting from the maximal SBR and the perfusion periods (Fig. 3B). Regions of interest (ROIs) were drawn on five selected vessels in NIR-II dynamic imaging performed for 30 min. On the basis of the ROIs, the SBR values for the five ROIs drawn were from 1.3 to 7.6 (Fig. 3, C and D). We further assessed the ability of the high brightness of the IR-783@BSA complex to afford light-emitting diode (LED)–excited NIR-II imaging. The clear hindlimb imaging was recorded over 1300 nm with an equal vessel-to-muscle signal ratio compared with 785-nm laser (10 to 50 mW/cm^2) excited imaging (Fig. 3, E to H). Collectively, these data indicated that the design of the prolonged IR-783@BSA complex afforded impressive blood vessel resolution and expanded time window, compared with free cyanine dyes (Fig. 3I). The superbright IR-783@BSA complex has great potential to translate NIR-II imaging into a clinical setting.

After administration of IR-783@BSA, NIR-II microscopy imaging of mouse brains in the NIR-II window afforded much clearer delineation of vasculature compared with the images from the NIR-I window, with approximately twofold enhancement of SBR (Fig. 4, A and B). Compared with the in vivo NIR-II whole-body (2.5×) images of shaved mouse heads at <30 min p.i. of the IR-783@BSA complex, the NIR-II microscopy images had better resolution, illuminating vessels that were as small as 3 μm (Fig. 4C). Vessel-to-normal tissue ratio statistics of both IR-783@BSA complex and free IR-783 images indicated that

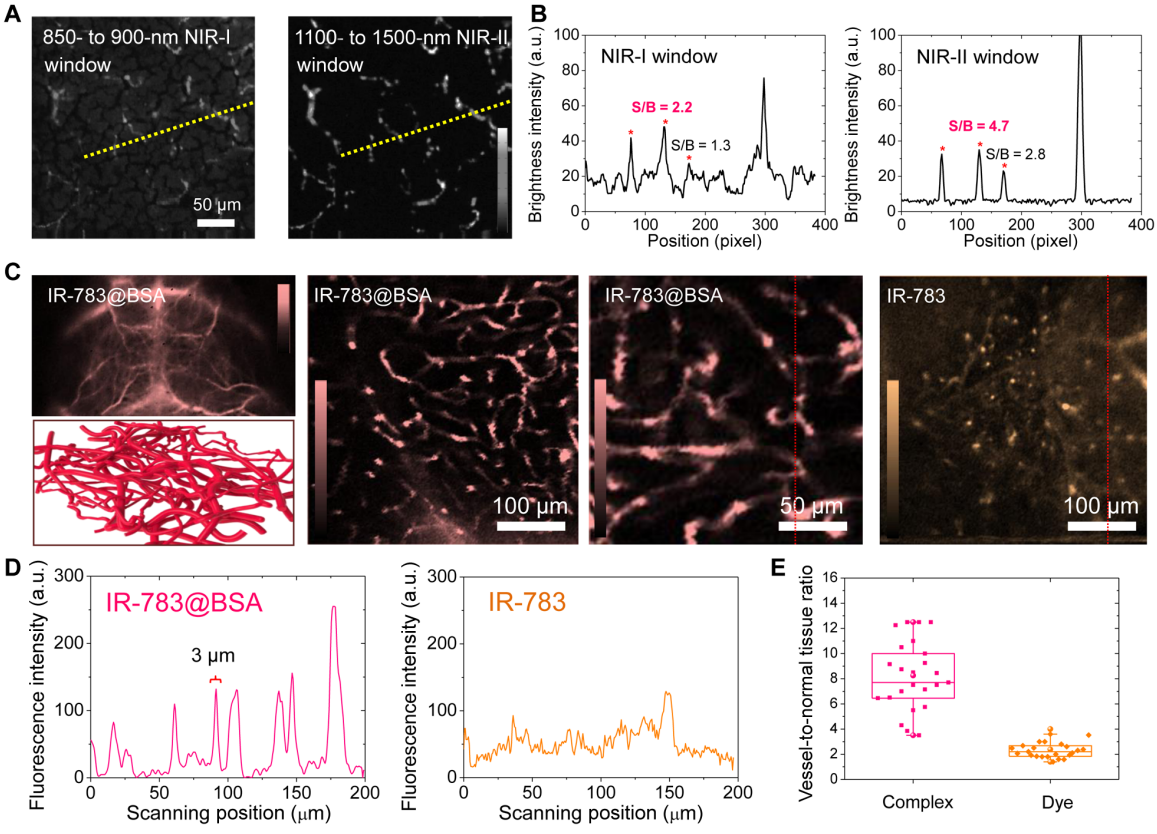

Fig. 4. NIR-II microscope imaging of the IR-783@BSA complex affords high-performance vessel imaging with both high resolution and contrast. (**A**) Ex vivo NIR-II microscope imaging of mouse brains at 1 hour p.i. of IR-783@BSA at both NIR-I and NIR-II windows. (**B**) Cross-sectional intensity profile of both NIR-I and NIR-II images at the same position. NIR-II imaging affords two times enhancement of SBR. (**C**) In vivo NIR-II whole-body (2.5×), vessel scheme and ex vivo microscope imaging of shaved/sectioned mouse head/brains after IR-783@BSA complex administration over 1300- and 1200-nm long-pass filters, respectively. (**D**) Cross-sectional intensity profile of both IR-783@BSA complex and free IR-783 images. (**E**) Vessel–to–normal tissue ratio statistics of both IR-783@BSA complex and free IR-783 images indicated that the IR-783@BSA complex exhibited super vessel imaging capacity.

the IR-783@BSA complex exhibited superior vessel imaging capacity in the NIR-II microscope approach (Fig. 4, D and E). The broad emission of the IR-783@BSA complex also potentially enables two-photon imaging with peak emission in the NIR-I window.

The dye-protein complexation strategy can be extended to antibodies for molecular targeted cancer imaging

Molecular imaging in the NIR-II window with remarkable SBR ratio and deep tissue penetration could provide a more holistic view of cancer marker expression to guide therapeutic management (*36*). Prompted by the promising results of the IR-783@BSA complex, we developed an IR-783@Erbitux complex for NIR-II molecular targeted imaging. The complex of antibody and dye can afford targeted imaging in the NIR-II window, with comparable NIR-II fluorescence labeling with the typical conjugation method (fig. S10, A and B) (*37*). We tested the targeting ability of the IR-783@Erbitux complex with both positive squamous cell carcinoma (SCC) cell and negative U87 cell lysate assays, indicating that a screened reaction condition with 60°C exhibited a high fluorescence brightness without loss of the high targeting affinity of Erbitux to its receptor (Fig. 5A and fig. S10, C to E). Comparison between the IR-783@Erbitux complex and a previous IR-FGP@Erbitux conjugate indicated that the IR-783@Erbitux complex exhibited improved SBR compared with the IR-FGP@Erbitux conjugate (fig. S10, F and G) (*37*), primarily because of the increased brightness of IR-783. SCC cell staining by IR-783@Erbitux described the maintained targeting ability of an antibody-based complex (Fig. 5B). In vivo NIR-II imaging of SCC tumor–bearing mice following tail vein injection of the IR-783@Erbitux complex and free IR-783 demonstrated the great targeting ability of the developed IR-783@Erbitux (Fig. 5, C and D). The NIR-II tumor signal of both IR-783@Erbitux was two- to threefold higher than that of free IR-783 by 24 hours p.i. (Fig. 5E). Although the liver uptake is higher than the albumin-based complex

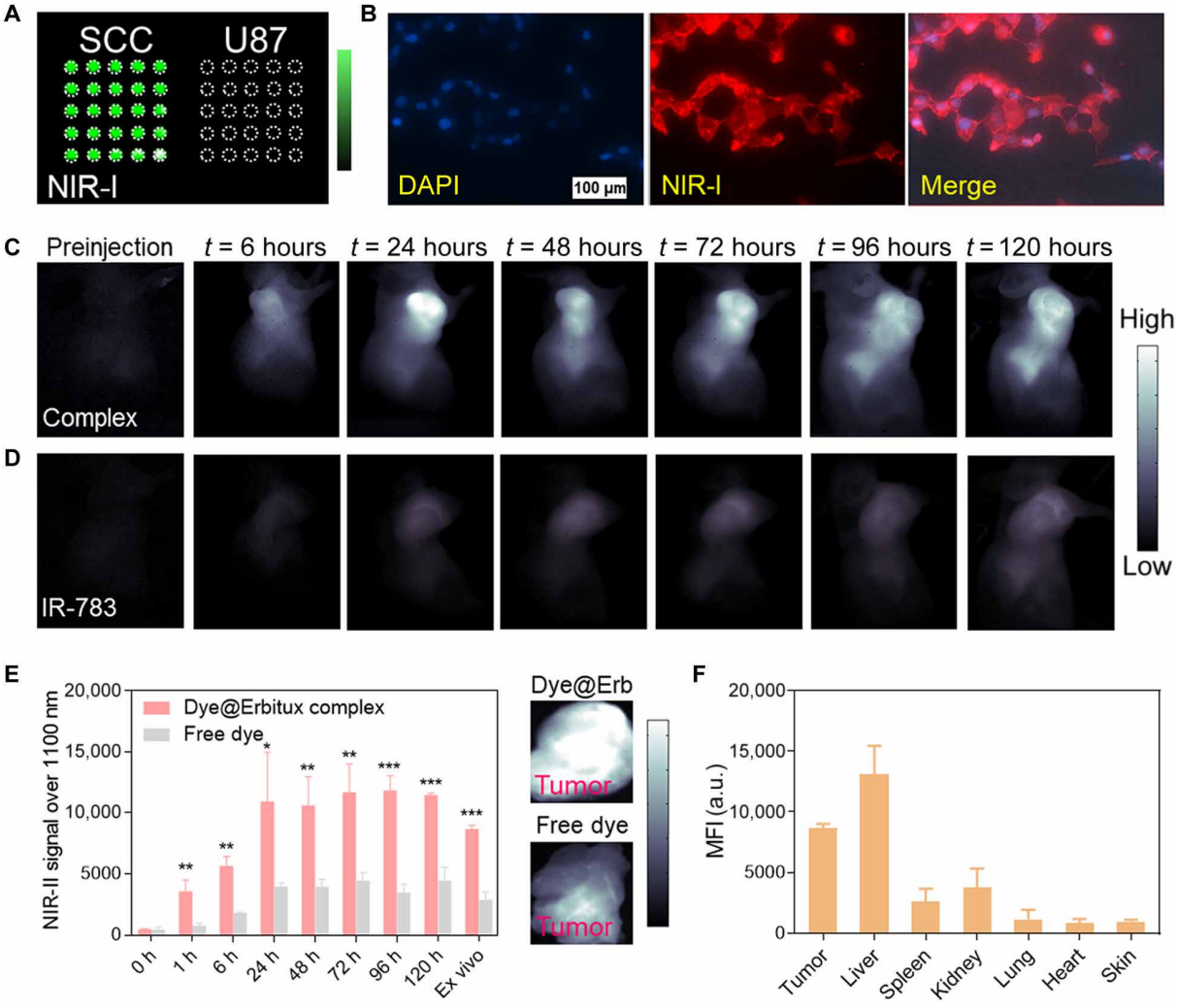

Fig. 5. The complex of antibody and dye can afford to target imaging in the NIR-II window. (**A**) Cell assay (lysate) test of the IR-783@Erbitux complex at both positive SCC cell and negative U87 cell. (**B**) SCC cell staining of IR-783@Erbitux described the reserved targeting ability of an antibody-based complex. DAPI, 4′,6-diamidino-2-phenylindole. (**C**) In vivo NIR-II imaging of an SCC tumor–bearing mouse with tail vein injection of the IR-783@Erbitux complex. (**D**) In vivo NIR-II imaging of an SCC tumor–bearing mouse with tail vein injection of free IR-783 under the same imaging conditions as the IR-783@Erbitux case. (**E**) NIR-II tumor signal of both IR-783@Erbitux and free IR-783 at increasing time points p.i. (significant difference between two groups was shown as $^{*}P < 0.05$, $^{**}P < 0.01$, and $^{***}P < 0.001$). Insets show tumors from different treatment cohorts with a lower *z* scale. (**F**) Ex vivo biodistribution of the IR-783@Erbitux complex at 168-hour time points p.i. MFI, mean fluorescence intensity.

and imaging quality is not sufficient, IR-783@Erbitux is still promising for achieving a facile molecular imaging platform (Fig. 5F). Collectively, this complexation shows potential to be expanded to the functional bio-supramolecules embedded with fluorophores, rendering multifunction with superior imaging capacity.

DISCUSSION

The motivation for NIR-II fluorescence-based biomedical imaging is better penetration depth and contrast resolution in imaging-navigation surgery compared to the existing NIR-I systems. When performing fluorescence imaging, laser-biological tissue interactions resulting from interacting excitation light, interface reflection, scattering, absorption, and autofluorescence all contribute to the loss of imaging signal and the inevitable yields of background noise. Great advantages exist by using NIR-II fluorescence imaging with reduced scattering coefficients across virtually all tissue types at longer wavelengths. It is highly promising to extend clinical image-guided surgery into the NIR-II/short-wave infrared range.

Current NIR-I fluorescence navigation systems are either open imaging platforms with vision hardware attached to an articulating arm or endoscope-based systems for endoscopic and laparoscopic/robotic surgery (*38*, *39*). The excitation/emission wavelengths of these systems are fixed to the visible–NIR-I range and typically only accommodate ICG-based detection. However, advancements in instrumentation now provide support for both ICG and IRDye-800CW. This is substantial, considering the number of clinical trials that make use of IRDye800CW. While traditional NIR-I imaging with ICG/IRDye800CW has yielded promising results in open, laparoscopic and robot-assisted surgery, it remains critically important to improve imaging detection depth, signal contrast, and sensitivity to produce a comprehensive fluorescence-guided platform capable of meeting all surgical requirements. The developed IR-783@BSA complex has sufficient fluorescent brightness in both the NIR-I and NIR-II region that adding indium gallium arsenide (InGaAs) sensors to existing fluorescence imaging platforms could facilitate infrared detection across a broad region of the electromagnetic spectrum (~700 to 1700 nm). A broad-spectrum infrared imaging platform incorporating both silicon and InGaAs sensors would offer surgeons the ability to toggle between high fluorescent brightness at traditional NIR wavelengths and high contrast/resolution in the NIR-II region.

The deeper tissue penetration and reduced autofluorescence of NIR-II imaging serve as the impetus for repurposing conventional NIR-I cyanine dyes for NIR-II applications. By systematically tailoring the supramolecular assembly of cyanine dyes with serum albumin, we identified a superior-performance complex with prolonged circulation time and excellent relative QY. Our investigations shed light into the mechanism of BSA-derived complex engagement with cyanine dyes and provide support for improving pharmacokinetics of cyanine dyes. Many attempts have been made to increase fluorescence intensity of NIR-II dyes, including developing rigid conformation of fluorophores. One important solution, as we reported here, is to introduce a protein scaffold to stabilize the relatively flexible fluorophores to reduce the nonradiation processes. By lodging in the pocket of albumin, the fluorophores would provide fluorescence enhancement due to a decreased internal rotation of the dye molecules. The protein scaffold usually holds some large conjugate group—such as tryptophan, phenylalanine, and tyrosine (Trp^{214} in this study)—to bind dyes with high affinity and provide π-electronic orbital hybridization with the dye molecule.

We optimized formation conditions for the fluorophore@BSA complex by applying a combination of GSH, GTD, and heat. In doing so, we obtained a self-assembling IR-783@BSA complex with sizes of sub–100 nm, with high stability and fluorescence intensity that enabled high-contrast blood vessel imaging with a ~3-hour imaging window. Vessel imaging was achieved for ex vivo microscopy, as well as for in vivo whole-body imaging, illuminating vessels as small as 3 μm. We also applied our design to the antibody system, with EGFR targeted imaging facilitated by an IR-783@Erbitux complex. This platform can potentially be extended to other molecular targets for personalized treatments. This innovation in NIR-II imaging of protein-complexed cyanine dyes with enhanced circulation time and imaging contrast have kept pace with new molecular targeting advances. These include full-color infrared imaging in both the NIR-I and NIR-II window to guide accurate transection/excision (*1*). With enhanced commercial infrared imaging fluorophores, augmented reality fluorescence visualization, and future NIR-I/II imaging platforms, parallel improvements across instrumentation and chemistry seem likely poised to fundamentally alter the manner in which surgeons visualize human anatomy.

MATERIALS AND METHODS

Materials

IR-783 was purchased from Sigma-Aldrich. IR-12N3 was purchased from Nirmidas Biotech Co. ICG (modified) for human injection was purchased from Dandong Yichuang Pharmaceutical Co. Ltd. PBS was purchased from HyClone. Erbitux (cetuximab) (2 mg/ml) was purchased from ImClone Systems Inc. BSA was purchased from Sigma-Aldrich. FBS was purchased from Neuromics. Sucrose was purchased from Sigma-Aldrich.

Cyanine@protein complex

BSA was dissolved in 1 × PBS with a concentration of 40 mg/ml (602 μM). IR-783 (IR-12N3 and ICG) was dissolved in dimethyl sulfoxide (DMSO) at 26.7 mM. GSH was dissolved in 15% DMSO/PBS buffer at a concentration of 0.25 M. GTD was dissolved in PBS at a concentration of 0.25 M. For a typical reaction, 500 μl of BSA was first added in 500 μl of PBS. Then, for four reaction conditions (freely mixed, GSH, GSH + GTD, and GTD), we added the needed GSH, GTD, or GSH/GTD. In detail, 60 μl of the GSH was added into the solution for condition 2 reaction. Sixty microliters of the GSH plus 24 μl of the GTD were added into the solution for condition 3 reaction. Twenty-four microliters of the GTD was added into the solution for condition 4 reaction. The suspension was vortexed for 30 s. After that, 11 μl of the IR-783 (26.7 mM) was added into the four conditions, respectively; the suspension was under shaker reaction at 37°C for 24 hours. Then, the complex was washed with Amicon Centrifugal Filter (30 kDa) five times against a PBS buffer. Last, the complex was heated at room temperature, 50°, 60°, and 70°C for 10 min, respectively. The reaction time, BSA-to-dye ratio, and reaction concentration were further optimized at different specific steps (figs. S3 and S4).

Bioconjugation between IR-FGP and Erbitux based on click chemistry (*37*)

1. Linker: Erbitux was reacted with dibenzocyclooctyne-(polyethylene glycol) 4-N-hydroxysuccinimidyl ester (DBCO-PEG4-NHS) cross-linker.

2. Reaction buffer: All of the reaction was carried out in 1 × PBS. The optimal ratio of Erbitux/dye/linker is 1:10:20.

3. First step: For a typical reaction, 300 μl of Erbitux (13.7 μM) and 26.7 μl of DBCO-PEG4-NHS (3.08 mM in DMSO) were mixed. The mixture was vortexed, followed by incubation at a shaker or stirring through magnetic beads for 2 hours.

4. Washing: After the reaction, the product was washed by the Amicon Centrifugal Filter (30 kDa) four times against a PBS buffer. The final volume is 300 μl.

5. Second step: Add 101 μl of IR-FGP (408.5 μM) to 100 μl of Erbitux-DBCO (the concentration of the dye can be tuned). The mixture was vortexed, followed by incubation at a shaker or stirring through magnetic beads for 3 hours.

6. The product (the output can be enlarged on the basis of the same ratio) was subjected to DGU purification. Sucrose column gradient for 4 ml of DGU tube was made by interval adding (10, 15, 20, 25, 30, 35, and 40%; 400 μl of each), tilt-permeated, and then subjected to ultracentrifuge for 18 hours at 50,000 rpm at 4°C.

7. The DGU sample was collected by fractionating.

Characterization

Dynamic light scattering and zeta potential measurements were conducted using a HORIBA nanoparticle analyzer SZ-100. An ultraviolet-visible-NIR spectrophotometer (Cary 6000i) with background correction was used to measure the optical absorption spectrum. Fluorescence spectrophotometry was carried out on a Hitachi F-7000 fluorescence spectrophotometer. Fluorescence microscopy was performed on an Olympus fluorescence microscope. NIR-I imaging was performed on a CRi Maestro in vivo imaging system with 100-ms exposure time.

NIR-II imaging

Mice were shaved using Nair hair removal cream (Nair Lotion with Aloe & Lanolin) and anesthetized using isoflurane before placing them in a stage with a venous catheter for injection of imaging agents. For each imaging experiment, at least three mice were used per group. All NIR-II images were collected on a two-dimensional InGaAs array (Princeton Instruments) based on a previous setup (*15*, *36*). The excitation laser was an 808-nm laser setup at a power density of ~0.15 W/cm^2. Emission was typically collected with different short/long-pass filters. A lens set was used for obtaining tunable magnifications, ranging from 1× (whole body) to 2.5× (high magnification) by changing the relative position of two NIR achromats (200 and 75 mm; Thorlabs). A variable exposure time was used for the InGaAs camera to capture images in the NIR-II window. NIR-II microscopy was built on the basis of the previous report, and the excitation laser was a 785-nm laser setup (*36*). PCA was performed on groups of images by considering each pixel to be an observation that varies over the variable time. We further programmed a MATLAB command to resolve the vein and artery information. The signals in the blood vessels from the beginning of injection were completely recorded, and the profile of each blood vessel perfusion was recorded. Since intravenous injection was performed, the venous vessels were firstly detected (the venous vessels were perfused with fluorophores after injection), followed by the artery vessels. For the calculation of vessel/muscle ratio, ROIs were drawn on selected vessels and the same muscle regions. Thus, the signal intensity of vessel to that of specific muscle ratio (SBR) value was required to compare the contrasts of different fluorophores.

Animals

All animal studies were conducted in accordance with the principles and procedures outlined in the National Institutes of Health (NIH) *Guide for the Care and Use of Laboratory Animals* and under protocols approved by the NIH Clinical Center Animal Care and Use Committee (protocol number: NIBIB 16-03). Some animal experiments were performed under the Stanford University's Administrative Panel on Laboratory Animal Care. Nude, C57, and BALB/c mice were purchased from the Jackson Laboratory (Bar Harbor, ME). Bedding, nesting material, food, and water were provided ad libitum. Ambient temperature was controlled at 20° to 22°C with 12-hour light/12-hour dark cycles. SCC tumors were formed by inoculating 1.5×10^6 SCC cells subcutaneously in nude mice.

Docking modeling

The structure of albumin for docking was prepared from the following processes:

1. Initial structure was from the RCSB website [Protein Data Bank (PDB) ID: 1E78].

2. The structure was solvated and neutralized in a TIP3P water box with a 12 Å buffering space at each side generated from the CHARMM-GUI.org website, while the disulfide bonds were not patched to generate the disulfide bond breaking protein.

3. One-nanosecond equilibrium in isothermal–isobaric ensemble (NPT) at 333.15 K (60°C).

4. Three-nanosecond production run in NPT ensemble at 333.15 K (60°C).

5. Remove solvation molecules.

At the docking stage, the protein was centered at the origin, and a 30 Å by 30 Å by 30 Å searching space was set for best performance. Nine best docking modes were achieved from a 3-ns molecular dynamics (MD) simulation.

Calculation for binding affinity

Because of the necessity of breaking the disulfide bonds in the albumin, the conformation of the albumin was obtained from a 3-ns MD equilibrium in the water box after the patching for the disulfide cleavages to the crystal structure from PDB (PDB ID: 1E78). The PDBQT files for the dye molecule and the albumin were both prepared using MGLTools. Furthermore, as a blind prediction, we searched all the space of the albumin; i.e., the sizes in the *X*, *Y*, and *Z* dimensions were set to include all the space. The same calculation step was repeated 100 times to find out the optimal pose. The binding affinities were all obtained by docking simulation from AutoDock Vina.

Docking for self-assembly

Starting from a 50 Å by 50 Å by 50 Å water box, the same number (nine) of dye molecules was included and fully equilibrated. Then, three repeated 1-ns NVT production runs were performed to generate 1000 snapshots from each 1-ps time step for IR-783 and ICG molecules, respectively. The radial distribution function analysis for the dye molecules (IR-783 and ICG) was performed on the given snapshots, which shows that ICG has a higher tendency for self-assembly.

DFT calculations

We carried out the DFT calculations to examine the electronic structure of IR-783. The ground state (S_0) geometries of the molecules were optimized using the B3LYP/6-31G(d) method with the GD3GJ dispersion correction. The corresponding range-separation parameter (ω, in bohr^{-1}) for IR-783 was optimally tuned on the basis of the long-range corrected LC-BLYP functional with the 6-31G(d)

basis set through the "GAP-tuning" procedure [see (*28*, *40*) for more details] using the nonequilibrium polarizable continuum model (PCM) to simulate the solvent environment, and the optimal ω value is 0.077 $bohr^{-1}$ for IR-783. We refer to the LC-BLYP functional with the optimally tuned ω value as LC-BLYP*. The excited state (S_1) properties of IR-783 were obtained using the time-dependent PCM-LC-BLYP*/6-31G(d) method. The HOMO and LUMO distributions were represented using VMD program. All the DFT calculations were performed using Gaussian 16 code (*40*).

Fluorescence enhancement calculation

Integration equation formalism PCM (IEFPCM) was used throughout the calculation to simulate the solvent environment. TDDFT was used to compute the excited state property of the dye molecule in both free state and bound state.

For the free-state excited state properties, to calculate the vertical excitation energy, a geometry optimization was performed at the ground state at the theoretical level of B3LYP/6-31G(d) with the GD3GJ dispersion correction including the equilibrium solvent. Then, a single point calculation of the optimized geometry was performed at the tuned LC-BLYP/6-31G(d) method in the equilibrium solvent model to obtain the equilibrium ground state energy [E(GS|Eq)]. The vertical excited state calculation with the state-specific nonequilibrium solvent model was performed using the tuned TD-LC-BLYP/6-31G(d) method thereafter to obtain the vertical excited state energy [E(ES|NEq)]. Last, the nonequilibrium vertical excitation energy was obtained as E(ES|NEq) – E(GS|Eq). To calculate the emission energy, the geometry of the dye molecule was optimized at the first singlet excited state at the level of the tuned TD-LC-BLYP/6-31G(d) method in the equilibrium IEFPCM solvent model, and the equilibrium excited state energy [E(ES|Eq)] was obtained. Then, state-specific equilibrium solvation of the excited state at first excited state optimized geometry was performed to record the solvation data for the next step. Last, by reading the solvation data from the previous step, the ground state energy with nonequilibrium solvation [E(GS|NEq)] was computed using the tuned LC-BLYP/6-31G(d) method. The nonequilibrium emission energy was computed as E(ES|Eq) – E(GS|NEq).

For the bound-state excited state properties, we first performed the geometry preparation. Specifically, from the optimal docking pose obtained from the 100 repeated docking simulations, we removed all atoms except for the dye molecule and the Trp^{214} residue and added all missing hydrogens for the following steps. To calculate the vertical excitation energy, we first performed the ground state energy calculation in equilibrium solvent to obtain the equilibrium ground state energy E(GS|Eq) and recorded the solvent data in the ground state. The vertical excited state calculation with the state-specific nonequilibrium solvent model was performed using the tuned TD-LC-BLYP/6-31G(d) method thereafter to obtain the vertical excited state energy [E(ES|NEq)]. Last, the nonequilibrium vertical excitation energy was obtained as E(ES|NEq) – E(GS|Eq). To study the emission excitation energy, we performed the state-specific equilibrium solvation of the excited state at first excited state optimized geometry, and we recorded the solvation data for the next step. By reading the solvation data from the previous step, the ground state energy with nonequilibrium solvation [E(GS|NEq)] was computed using the tuned LC-BLYP/6-31G(d) method. Last, the nonequilibrium emission energy was computed as E(ES|Eq)-E(GS|NEq).

SUPPLEMENTARY MATERIALS

Supplementary material for this article is available at http://advances.sciencemag.org/cgi/content/full/5/9/eaaw0672/DC1

Fig. S1. Relative QYs of IR-783, IR-12N3, and ICG in BSA/FBS, depicted by the slope of fluorescence intensity versus absorption.
Fig. S2. Method optimization for the fluorophore@BSA complex.
Fig. S3. The optimization for ratio and reaction concentration of BSA and IR-783.
Fig. S4. Stability, brightness, and size of the IR-783@BSA complex at 1:0.5, 1:1, and 1:2 ratios.
Fig. S5. Docking simulation and computational modeling demonstrating the binding poses and the mechanism of increased QY for complexation.
Fig. S6. The free IR-12N3/ICG/IR-783 has quick hepatobiliary clearance and short imaging window compared to their complex with albumin.
Fig. S7. Comparison of the vessel imaging time window of free IR-783 with the IR-783@BSA complex.
Fig. S8. Further imaging comparison of IR-783@BSA from different conditions (C2, C3, and C4).
Fig. S9. NIR-II QY of the IR-783@BSA complex and NIR-II vessel imaging in whole-body mode.
Fig. S10. The IR-783@Erbitux complex afforded an efficient conjugate and decent targeting ability for molecular imaging.
Table S1. The excitation energies for both vertical excitation and emission computed using TDDFT/IEFPCM in complex mode.
References (*41*–*52*)

REFERENCES AND NOTES

1. A. L. Vahrmeijer, M. Hutteman, J. R. van der Vorst, C. J. van de Velde, J. V. Frangioni, Image-guided cancer surgery using near-infrared fluorescence. *Nat. Rev. Clin. Oncol.* **10**, 507–518 (2013).
2. H. Chen, X. Tong, L. Lang, O. Jacobson, B. C. Yung, X. Yang, R. Bai, D. O. Kiesewetter, Y. Ma, H. Wu, G. Niu, X. Chen, Quantification of tumor vascular permeability and blood volume by positron emission tomography. *Theranostics* **7**, 2363–2376 (2017).
3. C. Vinegoni, I. Botnaru, E. Aikawa, M. A. Calfon, Y. Iwamoto, E. J. Folco, V. Ntziachristos, R. Weissleder, P. Libby, F. A. Jaffer, Indocyanine green enables near-infrared fluorescence imaging of lipid-rich, inflamed atherosclerotic plaques. *Sci. Transl. Med.* **3**, 84ra45 (2011).
4. G. Hong, A. L. Antaris, H. Dai, Near-infrared fluorophores for biomedical imaging. *Nat. Biomed. Eng.* **1**, 0010 (2017).
5. J. Qi, C. Sun, A. Zebibula, H. Zhang, R. T. K. Kwok, X. Zhao, W. Xi, J. W. Y. Lam, J. Qian, B. Z. Tang, Real-time and high-resolution bioimaging with bright aggregation-induced emission dots in short-wave infrared region. *Adv. Mater.* **30**, e1706856 (2018).
6. X. Dang, L. Gu, J. Qi, S. Correa, G. Zhang, A. M. Belcher, P. T. Hammond, Layer-by-layer assembled fluorescent probes in the second near-infrared window for systemic delivery and detection of ovarian cancer. *Proc. Natl. Acad. Sci. U.S.A.* **113**, 5179–5184 (2016).
7. K. Welsher, Z. Liu, S. P. Sherlock, J. T. Robinson, Z. Chen, D. Daranciang, H. Dai, A route to brightly fluorescent carbon nanotubes for near-infrared imaging in mice. *Nat. Nanotechnol.* **4**, 773–780 (2009).
8. Y. Jiang, K. Pu, Advanced photoacoustic imaging applications of near-infrared absorbing organic nanoparticles. *Small* **13**, 1700710 (2017).
9. Kenry, Y. Duan, B. Liu, Recent advances of optical imaging in the second near-infrared window. *Adv. Mater.* **30**, e1802394 (2018).
10. X.-D. Zhang, H. Wang, A. L. Antaris, L. Li, S. Diao, R. Ma, A. Nguyen, G. Hong, Z. Ma, J. Wang, S. Zhu, J. M. Castellano, T. Wyss-Coray, Y. Liang, J. Luo, H. Dai, Traumatic brain injury imaging in the second near-infrared window with a molecular fluorophore. *Adv. Mater.* **28**, 6872–6879 (2016).
11. B. Li, L. Lu, M. Zhao, Z. Lei, F. Zhang, An efficient 1064 nm NIR-II excitation fluorescent molecular dye for deep-tissue high-resolution dynamic bioimaging. *Angew. Chem. Int. Ed.* **57**, 7483–7487 (2018).
12. S. He, J. Song, J. Qu, Z. Cheng, Crucial breakthrough of second near-infrared biological window fluorophores: Design and synthesis toward multimodal imaging and theranostics. *Chem. Soc. Rev.* **47**, 4258–4278 (2018).
13. A. L. Antaris, H. Chen, S. Diao, Z. Ma, Z. Zhang, S. Zhu, J. Wang, A. X. Lozano, Q. Fan, L. Chew, M. Zhu, K. Cheng, X. Hong, H. Dai, Z. Cheng, A high quantum yield molecule-protein complex fluorophore for near-infrared II imaging. *Nat. Commun.* **8**, 15269 (2017).
14. J. A. Carr, D. Franke, J. R. Caram, C. F. Perkinson, M. Saif, V. Askoxylakis, M. Datta, D. Fukumura, R. K. Jain, M. G. Bawendi, O. T. Bruns, Shortwave infrared fluorescence imaging with the clinically approved near-infrared dye indocyanine green. *Proc. Natl. Acad. Sci. U.S.A.* **115**, 4465–4470 (2018).
15. S. Zhu, Z. Hu, R. Tian, B. C. Yung, Q. Yang, S. Zhao, D. O. Kiesewetter, G. Niu, H. Sun, A. L. Antaris, X. Chen, Repurposing cyanine NIR-I dyes accelerates clinical translation of near-infrared-II (NIR-II) bioimaging. *Adv. Mater.*, e1802546 (2018).
16. G. Deng, S. Li, Z. Sun, W. Li, L. Zhou, J. Zhang, P. Gong, L. Cai, Near-infrared fluorescence imaging in the largely unexplored window of 900-1,000 nm. *Theranostics* **8**, 4116–4128 (2018).

17. S. Zhu, B. C. Yung, S. Chandra, G. Niu, A. L. Antaris, X. Chen, Near-infrared-II (NIR-II) bioimaging via off-peak NIR-I fluorescence emission. *Theranostics* **8**, 4141–4151 (2018).
18. M. Yu, J. Liu, X. Ning, J. Zheng, High-contrast noninvasive imaging of kidney clearance kinetics enabled by renal clearable nanofluorophores. *Angew. Chem. Int. Ed.* **54**, 15434–15438 (2015).
19. H. Kang, J. Gravier, K. Bao, H. Wada, J. H. Lee, Y. Baek, G. El Fakhri, S. Gioux, B. P. Rubin, J.-L. Coll, H. S. Choi, Renal clearable organic nanocarriers for bioimaging and drug delivery. *Adv. Mater.* **28**, 8162–8168 (2016).
20. X. Zeng, Y. Xiao, J. Lin, S. Li, H. Zhou, J. Nong, G. Xu, H. Wang, F. Xu, J. Wu, Z. Deng, X. Hong, Near-infrared II dye-protein complex for biomedical imaging and imaging-guided photothermal therapy. *Adv. Healthc. Mater.* **7**, e1800589 (2018).
21. Z. Liu, X. Chen, Simple bioconjugate chemistry serves great clinical advances: Albumin as a versatile platform for diagnosis and precision therapy. *Chem. Soc. Rev.* **45**, 1432–1456 (2016).
22. G. Zhu, G. M. Lynn, O. Jacobson, K. Chen, Y. Liu, H. Zhang, Y. Ma, F. Zhang, R. Tian, Q. Ni, S. Cheng, Z. Wang, N. Lu, B. C. Yung, Z. Wang, L. Lang, X. Fu, A. Jin, I. D. Weiss, H. Vishwasrao, G. Niu, H. Shroff, D. M. Klinman, R. A. Seder, X. Chen, Albumin/vaccine nanocomplexes that assemble in vivo for combination cancer immunotherapy. *Nat. Commun.* **8**, 1954 (2017).
23. R. Tian, H. Ma, Q. Yang, H. Wan, S. Zhu, S. Chandra, H. Sun, D. O. Kiesewetter, G. Niu, Y. Liang, X. Chen, Rational design of a super-contrast NIR-II fluorophore affords high-performance NIR-II molecular imaging guided microsurgery. *Chem. Sci.* **10**, 326–332 (2018).
24. T. Ueki, Y. Hiragi, M. Kataoka, Y. Inoko, Y. Amemiya, Y. Izumi, H. Tagawa, Y. Muroga, Aggregation of bovine serum albumin upon cleavage of its disulfide bonds, studied by the time-resolved small-angle X-ray scattering technique with synchrotron radiation. *Biophys. Chem.* **23**, 115–124 (1985).
25. N. Ohta, D. Chen, S. Ito, T. Futo, T. Yotsuyanagi, K. Ikeda, Effect of *trans*-diamminedichloroplatinum(II) on human serum albumin: Conformational changes through partial disulfide bond cleavage. *Int. J. Pharm.* **118**, 85–93 (1995).
26. M. Y. Berezin, H. Lee, W. Akers, G. Nikiforovich, S. Achilefu, Ratiometric analysis of fluorescence lifetime for probing binding sites in albumin with near-infrared fluorescent molecular probes. *Photochem. Photobiol.* **83**, 1371–1378 (2007).
27. J. M. Jean, K. B. Hall, 2-Aminopurine fluorescence quenching and lifetimes: Role of base stacking. *Proc. Natl. Acad. Sci. U.S.A.* **98**, 37–41 (2001).
28. H. Sun, C. Zhong, J.-L. Brédas, Reliable prediction with tuned range-separated functionals of the singlet–triplet gap in organic emitters for thermally activated delayed fluorescence. *J. Chem. Theory Comput.* **11**, 3851–3858 (2015).
29. D. Ding, X. Tang, X. Cao, J. Wu, A. Yuan, Q. Qiao, J. Pan, Y. Hu, Novel self-assembly endows human serum albumin nanoparticles with an enhanced antitumor efficacy. *AAPS PharmSciTech* **15**, 213–222 (2014).
30. Z. Sheng, D. Hu, M. Zheng, P. Zhao, H. Liu, D. Gao, P. Gong, G. Gao, P. Zhang, Y. Ma, L. Cai, Smart human serum albumin-indocyanine green nanoparticles generated by programmed assembly for dual-modal imaging-guided cancer synergistic phototherapy. *ACS Nano* **8**, 12310–12322 (2014).
31. Q. Chen, C. Liang, C. Wang, Z. Liu, An imagable and photothermal "Abraxane-like" nanodrug for combination cancer therapy to treat subcutaneous and metastatic breast tumors. *Adv. Mater.* **27**, 903–910 (2015).
32. H. Kouchakzadeh, M. S. Safavi, S. A. Shojaosadati, Efficient delivery of therapeutic agents by using targeted albumin nanoparticles. *Adv. Protein Chem. Struct. Biol.* **98**, 121–143 (2015).
33. M. Karimi, S. Bahrami, S. B. Ravari, P. S. Zangabad, H. Mirshekari, M. Bozorgomid, S. Shahreza, M. Sori, M. R. Hamblin, Albumin nanostructures as advanced drug delivery systems. *Expert Opin. Drug Deliv.* **13**, 1609–1623 (2016).
34. Q. Yang, Z. Ma, H. Wang, B. Zhou, S. Zhu, Y. Zhong, J. Wang, H. Wan, A. Antaris, R. Ma, X. Zhang, J. Yang, X. Zhang, H. Sun, W. Liu, Y. Liang, H. Dai, Rational design of molecular fluorophores for biological imaging in the NIR-II window. *Adv. Mater.* **29**, 1605497 (2017).
35. A. L. Antaris, H. Chen, K. Cheng, Y. Sun, G. Hong, C. Qu, S. Diao, Z. Deng, X. Hu, B. Zhang, X. Zhang, O. K. Yaghi, Z. R. Alamparambil, X. Hong, Z. Cheng, H. Dai, A small-molecule dye for NIR-II imaging. *Nat. Mater.* **15**, 235–242 (2016).
36. S. Zhu, S. Herraiz, J. Yue, M. Zhang, H. Wan, Q. Yang, Z. Ma, Y. Wang, J. He, A. L. Antaris, Y. Zhong, S. Diao, Y. Feng, Y. Zhou, K. Yu, G. Hong, Y. Liang, A. J. Hsueh, H. Dai, 3D NIR-II molecular imaging distinguishes targeted organs with high-performance NIR-II bioconjugates. *Adv. Mater.* **30**, e1705799 (2018).
37. S. Zhu, Q. Yang, A. L. Antaris, J. Yue, Z. Ma, H. Wang, W. Huang, H. Wan, J. Wang, S. Diao, B. Zhang, X. Li, Y. Zhong, K. Yu, G. Hong, J. Luo, Y. Liang, H. Dai, Molecular imaging of biological systems with a clickable dye in the broad 800- to 1,700-nm near-infrared window. *Proc. Natl. Acad. Sci. U.S.A.* **114**, 962–967 (2017).
38. C. Chi, Y. Du, J. Ye, D. Kou, J. Qiu, J. Wang, J. Tian, X. Chen, Intraoperative imaging-guided cancer surgery: From current fluorescence molecular imaging methods to future multi-modality imaging technology. *Theranostics* **4**, 1072–1084 (2014).
39. R. M. Williams, C. Lee, T. V. Galassi, J. D. Harvey, R. Leicher, M. Sirenko, M. A. Dorso, J. Shah, N. Olvera, F. Dao, D. A. Levine, D. A. Heller, Noninvasive ovarian cancer biomarker detection via an optical nanosensor implant. *Sci. Adv.* **4**, eaaq1090 (2018).
40. M. J. Frisch, G. W. Trucks, H. B. Schlegel, G. E. Scuseria, M. A. Robb, J. R. Cheeseman, G. Scalmani, V. Barone, G. A. Petersson, H. Nakatsuji, X. Li, M. Caricato, A. Marenich, J. Bloino, B. G. Janesko, R. Gomperts, B. Mennucci, H. P. Hratchian, J. V. Ortiz, A. F. Izmaylov, J. L. Sonnenberg, D. Williams-Young, F. Ding, F. Lipparini, F. Egidi, J. Goings, B. Peng, A. Petrone, T. Henderson, D. Ranasinghe, V. G. Zakrzewski, J. Gao, N. Rega, G. Zheng, W. Liang, M. Hada, M. Ehara, K. Toyota, R. Fukuda, J. Hasegawa, M. Ishida, T. Nakajima, Y. Honda, O. Kitao, H. Nakai, T. Vreven, K. Throssell, J. A. Montgomery, Jr., J. E. Peralta, F. Ogliaro, M. Bearpark, J. J. Heyd, E. Brothers, K. N. Kudin, V. N. Staroverov, T. Keith, R. Kobayashi, J. Normand, K. Raghavachari, A. Rendell, J. C. Burant, S. S. Iyengar, J. Tomasi, M. Cossi, J. M. Millam, M. Klene, C. Adamo, R. Cammi, J. W. Ochterski, R. L. Martin, K. Morokuma, O. Farkas, J. B. Foresman, D. J. Fox, *Gaussian 16: Revision A.03* (Gaussian Inc., 2016).
41. T. J. Russin, E. I. Altinoğlu, J. H. Adair, P. C. Eklund, Measuring the fluorescent quantum efficiency of indocyanine green encapsulated in nanocomposite particulates. *J. Phys. Condens. Matter* **22**, 334217 (2010).
42. F.-F. An, X.-H. Zhang, Strategies for preparing albumin-based nanoparticles for multifunctional bioimaging and drug delivery. *Theranostics* **7**, 3667–3689 (2017).
43. J. Sowell, K. A. Agnew-Heard, J. C. Mason, C. Mama, L. Strekowski, G. Patonay, Use of non-covalent labeling in illustrating ligand binding to human serum albumin via affinity capillary electrophoresis with near-infrared laser induced fluorescence detection. *J. Chromatogr. B Biomed. Sci. Appl.* **755**, 91–99 (2001).
44. A. S. Tatikolov, S. M. Costa, Complexation of polymethine dyes with human serum albumin: A spectroscopic study. *Biophys. Chem.* **107**, 33–49 (2004).
45. F. M. Hamann, R. Brehm, J. Pauli, M. Grabolle, W. Frank, W. A. Kaiser, D. Fischer, U. Resch-Genger, I. Hilger, Controlled modulation of serum protein binding and biodistribution of asymmetric cyanine dyes by variation of the number of sulfonate groups. *Mol. Imaging* **10**, 258–269 (2011).
46. M. Saikiran, D. Sato, S. S. Pandey, T. Kato, Photophysical investigations of squaraine and cyanine dyes and their interaction with bovine serum albumin. *J. Phys. Conf. Ser.* **704**, 012012 (2016).
47. Y. Zhang, J. Xiang, Y. Tang, G. Xu, W. Yan, Chiral transformation of achiral J-aggregates of a cyanine dye templated by human serum albumin. *ChemPhysChem* **8**, 224–226 (2007).
48. M. Otagiri, V. T. G. Chuang, *Albumin in Medicine* (Springer Science, 2016).
49. P. Ma, R. J. Mumper, Paclitaxel nano-delivery systems: A comprehensive review. *J. Nanomed. Nanotechnol.* **4**, 1000164 (2013).
50. F. Kratz, B. Elsadek, Clinical impact of serum proteins on drug delivery. *J. Control. Release* **161**, 429–445 (2012).
51. S. Diao, J. L. Blackburn, G. Hong, A. L. Antaris, J. Chang, J. Z. Wu, B. Zhang, K. Cheng, C. J. Kuo, H. Dai, Fluorescence imaging in vivo at wavelengths beyond 1500 nm. *Angew. Chem. Int. Ed.* **54**, 14758–14762 (2015).
52. S. Zhu, R. Tian, A. L. Antaris, X. Chen, H. Dai, Near-infrared-II molecular dyes for cancer imaging and surgery. *Adv. Mater.* **32**, e1900321 (2019).

Acknowledgments: This work used the high-performance computational capabilities of the LoBoS in the Biochemistry and Biophysics Center Division of Intramural Research, National Heart, Lung, and Blood Institute of the NIH (www.lobos.nih.gov/LoBoS.shtml). We are indebted to H. Dai and E. L. Rosenthal (Stanford University) and Y. Liang, Q. Yang, K. Yu, and A. Jin for valuable suggestions and support. **Funding:** Support for this research was provided by the Intramural Research Program of the National Institute of Biomedical Imaging and Bioengineering (NIBIB), NIH. The National Natural Science Foundation of China (Grant Nos. 11727810) and the ECNU Multifunctional Platform for Innovation (001) for providing computational and storage resources. **Author contributions:** S.Z., R.T., and X.C. conceived and designed the study. R.T., S.Z., and S.C. performed all the experiments. Q.Z., Z. H., and H.S. performed the theoretical calculations. R.T., S.Z., J.L., S.C., R.E., K.H., T.T., G.N., D.O.K., X.Z., A.L.A., and B.R.B. analyzed data and wrote the manuscript. **Competing interests:** The authors declare that they have no competing interests. **Data and materials availability:** All data needed to evaluate the conclusions in the paper are present in the paper and/or the Supplementary Materials. Additional data related to this paper may be requested from the authors.

Submitted 14 November 2018
Accepted 15 August 2019
Published 13 September 2019
10.1126/sciadv.aaw0672

Citation: R. Tian, Q. Zeng, S. Zhu, J. Lau, S. Chandra, R. Ertsey, K. S. Hettie, T. Teraphongphom, Z. Hu, G. Niu, D. O. Kiesewetter, H. Sun, X. Zhang, A. L. Antaris, B. R. Brooks, X. Chen, Albumin-chaperoned cyanine dye yields superbright NIR-II fluorophore with enhanced pharmacokinetics. *Sci. Adv.* **5**, eaaw0672 (2019).